Available online at www.sciencedirect.com
ScienceDirect
Journal of Nuclear Materials 371 (2007) 1–17
journal of nuclear materials
www.elsevier.com/locate/jnucmat

Oxidation of ferritic–martensitic alloys T91, HCM12A and HT-9 in supercritical water

Pantip Ampornrat *, Gary S. Was

Nuclear Engineering and Radiological Sciences, University of Michigan, 2355 Bonisteel Blvd, Ann Arbor, MI 48109, USA

Abstract

The oxidation behavior of ferritic–martensitic (F–M) alloys in supercritical water (SCW) was studied in order to evaluate the suitability of these alloys for use in the Gen IV supercritical water reactor (SCWR) concept. A series of exposure tests in SCW were performed with three F–M alloys: T91, HCM12A, and HT-9. The effect of temperature was evaluated over the range of 400–600 °C and the dissolved oxygen concentration was controlled at <10 ppb (deaerated condition), 100 and 300 ppb. The oxidation behavior was determined from weight gain measurements along with oxide structure analysis. The results indicated that the oxidation rate was strongly dependent on temperature and followed an Arrhenius behavior. Activation energies for oxidation were 172, 177, and 189 kJ/mol for HT-9, HCM12A, and T91, respectively. The time dependence of the oxidation rate followed an exponential law with time exponents ~0.3–0.42. Reduction in oxidation rate was observed at intermediate values (100–300 ppb) of dissolved oxygen concentration. The oxide formed on the alloy surface consisted of an outer layer of porous magnetite (Fe_3O_4) and an inner layer of iron chromium oxide, $(Fe,Cr)_3O_4$ with spinel structure. A transition region lies beneath the inner oxide in which the metal content increases to bulk values and the oxygen content decreases to nearly zero. Iron chromium oxide, (Fe,Cr)O, with the wustite structure was observed in the transition layer at 600 °C. The relatively good agreement between the activation energies for oxidation and that for grain boundary diffusion of oxygen support an oxidation mechanism based on short circuit oxygen diffusion to the oxide–metal interface.

1. Introduction

The supercritical water reactor (SCWR) will operate above the critical point of water, in which 375 °C and 22.1 MPa [1,2]. Under these conditions, water is fluid with properties intermediate between those of a liquid and a gas. The properties affected include the density, hydrogen bonding, ionization product, dielectric constant, heat capacity, and the transport properties of water. These properties can have a very large impact on the corrosion properties of alloys. The density of SCW varies from around 0.1–0.8 g/cm^3 compares to the density of water as a liquid (1 g/cm^3) and a gas (0.001 g/cm^3) [3]. Since SCW can be considered as a dense gas, the density varies significantly with changes in temperature and pressure. Both the dielectric constant and the ionization product decrease dramatically when water passes into the critical region, implying that the oxidation rate in the sub-critical region should

* Corresponding author. Fax: +1 734 763 4540.
E-mail address: pantipam@umich.edu (P. Ampornrat).

0022-3115/$ - see front matter © 2007 Elsevier B.V. All rights reserved.
doi:10.1016/j.jnucmat.2007.05.023

be higher than that in the supercritical region [4]. However, since the temperature is expected to have a strong effect, the oxidation rate in SCW is not easily predicted. The corrosion experiments in this paper were designed to be comparable with the environment in an SCWR in which the temperature ranges up to 600 °C at a pressure of 24.1 MPa (3500 psi).

Ferritic–martensitic (F–M) alloys have been identified as candidates for fuel cladding and core structural components in the Generation IV SCWR concept. F–M alloys exhibit good high temperature strength and creep resistance, high thermal conductivity, low swelling and activation under irradiation, low susceptibility to stress corrosion cracking and modest corrosion resistance. While F–M alloys exhibit good resistance to IGSCC compared to austenitic alloys, their behavior following irradiation is unknown. Further, the corrosion rate under SCW conditions must be quantified in order to determine if these alloys can withstand the proposed operating environment of an SCWR.

Three F–M alloys, T91 (Fe–9Cr–MoVNb), HCM12A (Fe–12Cr–MoVNbW), and HT-9 (Fe–12Cr–MoVNi) were studied in this project. Alloy T91 has been widely used in non-nuclear application and HCM12A is a third generation alloy that was developed for higher creep strength. HT-9 is an early generation F–M alloy that has been proposed for nuclear applications due to its radiation stability.

Oxidation data on F–M alloys in SCW comes primarily from supercritical fossil plant experience, supercritical water oxidation (SCWO), and from very recent studies in support of the SCWR [5–10]. To obtain a better understanding of the oxidation behavior of F–M alloys in SCW, exposure experiments were conducted in a multi-sample supercritical water system (MSCW) at the University of Michigan. The corrosion coupons in each test included the three F–M alloys; T91, HCM12A and HT-9. The test conditions were controlled in order to study the effects of time, temperature and dissolved oxygen. The parameter range studied was for temperatures between 400 °C and 600 °C, exposure times between 188 h and 490 h, and dissolved oxygen (DO) concentrations between 10 ppb and 300 ppb. Measurements of exposure corrosion coupons yielded weight gain, oxide thickness, oxide composition profile, oxide morphology, and oxide crystal structure. The oxidation mechanism was determined from the activation energy and the oxidation rate of the experiments at 400, 500, and 600 °C and between 188 h and 490 h exposure in deaerated SCW.

2. Experiment

2.1. Materials

Alloy T91 (Fe–9Cr–MoVNb) contains 9% of chromium with major alloying elements Mo, V, and Nb. Alloy HCM12A (Fe–12Cr–MoVNbW) contains 11% chromium and alloying elements Mo, V, Nb, W with the addition of Cu for higher creep strength. Alloy HT-9 (Fe–12Cr–MoVNi) contains 12% Cr and Mo, V, and Ni. The chemical compositions of the three alloys are given in Table 1. All of the F–M alloys were prepared with the standard heat treatment consisting of annealing and tempering treatments as shown in Table 2. The microstructure and grain size resulting from heat treatment are as follows. T91 consists of tempered martensitic laths forming subgrains in a ferrite matrix with an approximate grain size of 9 μm [11]. The matrix structure of HCM12A is martensite as shown by the elongated, needle-like raised surfaces with the grain size of 13.5 μm [12]. The microstructure of HT-9 consists of relatively large, ~50 μm grains. Fig. 1 shows the SEM image of alloy T91.

After heat treatment, the as-received alloys were machined by electric discharge so that the long axis of the coupon was in the rolling direction. The corrosion coupon dimensions are 20 mm × 10 mm × 1 mm and each coupon has a small hole for securing it in the autoclave. The corrosion coupons were mechanically polished using standard mechanical

Table 1
Composition of the ferritic–martensitic alloys T91, HCM12A and HT-9

Alloy	Chemical composition (wt%)															
	C	Mn	P	S	Si	Ni	Cr	Mo	Cu	N	Co	Ti	Nb	Al	V	W
T91	0.10	0.45	0.009	0.003	0.28	0.21	8.37	0.90	0.17	0.048			0.076	0.022	0.216	
HCM12A	0.11	0.64	0.016	0.002	0.27	0.39	10.83	0.30	1.02	0.063			0.054	0.001	0.190	1.89
HT-9	0.20	0.52	0.020	0.006	0.22	0.50	11.63	1.00	0.04	0.047	0.08	<0.01		<0.01	0.300	0.52

Table 2
Heat treatment for the T91, HCM12A, and HT-9 materials used in this work

Alloy	Anneal			Tempering		
	Temp. (°C)	Time (min)	Cooling	Temp. (°C)	Time (min)	Cooling
T91	1066	46	Air cooled	790	42	Air cooled
HCM12A	1050	60	Air cooled	770	45	Air cooled
HT-9	1040	30	Air cooled	760	60	Air cooled

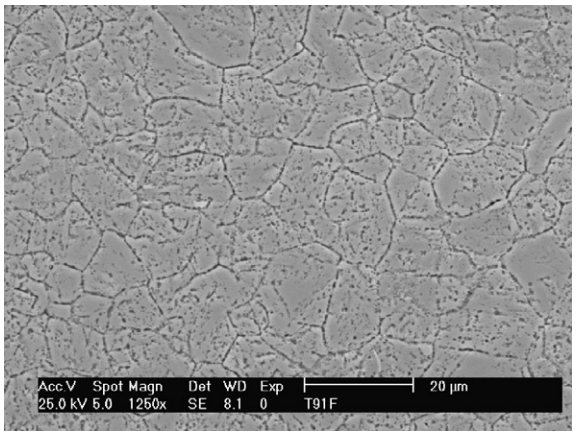

Fig. 1. Microstructure of T91 showing average grain size around 9 μm.

Table 3
Summary of corrosion experiments in SCW

Temperature (°C)	Exp. time (h)	Dissolved oxygen (ppb)	Outlet conductivity (μS/cm)
400 ± 5	151.5	Deaerated (<10)	0.075
400 ± 5	188.0	Deaerated (<10)	0.075
400 ± 5	136.4	Deaerated (<10)	0.075
400 ± 5	165.0	Deaerated (<10)	0.075
500 ± 5	182.2	Deaerated (<10)	0.075
500 ± 5	203.0	Deaerated (<10)	0.075
500 ± 5	236.0	100	0.1
500 ± 5	182.0	300	<1
600 ± 5	191.1	Deaerated (<10)	0.12

Note: Pressure inside test vessel was controlled at 24.8 ± 0.07 MPa.
Inlet conductivity was 0.06 μS/cm.

techniques and then electropolished in a solution of perchloric acid (10%) and methanol solution maintained at −30 °C and with an applied voltage of 35 V for 5–20 s to obtain a mirror finish. All of the corrosion coupons were prepared with a consistent surface finish.

2.2. SCW exposure experiments

Exposure tests were performed in the MSCW at the University of Michigan. The system consists of three major components; the water preparation column, the pressurizer and preheater, and the main vessel. Distilled water was passed through an ion exchange column and filter. The dissolved oxygen concentration was controlled by bubbling either pure argon gas for deaeration or a mixture of argon and oxygen. Dissolved oxygen was maintained below 10 ppb in the deaerated condition, and at 100 ± 10 and 300 ± 10 ppb DO in the controlled oxygen condition. The inlet conductivity was 0.06 mS/cm. The water was pressurized and passed through a preheater before being fed at a flow rate >50 ml/min to the test vessel heated to the target temperature. Water from test vessel was circulated back to the water preparation column, passing through an ion exchanger and filter. Samples were suspended at the same height in the autoclave using a wire of nickel-base alloy 600 with a zirconia ceramic insulator attached to the sample tree to avoid galvanic effects. Exposure tests were conducted over the temperature range of 400–600 °C, and at pressure of 24.8 ± 0.07 MPa (3600 ± 10 psig). During exposure, the temperature inside the autoclave was controlled to within ± 5 °C of the target temperature. The outlet conductivity was maintained between ~0.075 and 0.10 μS/cm. The increase in conductivity indicated the possibility of ion dissolution in SCW under the test conditions. Exposure times were ~160–200 h in each experiment. The time dependence of oxidation was studied at 400 °C with exposure times of 188, 324, and 490 h, and at 500 °C with exposure times of 182 and 385 h. A summary of experiment at conditions is given in Table 3.

2.3. Analysis methods

After completion of the exposure experiments, the corrosion coupons were characterized by weight

Table 4
Summary of exposure tests in 400 °C and 600 °C deaerated SCW, and in 500 °C deaerated SCW, containing 100 ppb DO, and 300 ppb DO

Temperature (°C)	400			500			600		
DO (ppb)	<10[a]			<10[a]			<10[a]		
Exposure (h)	151.5	151.5	151.5	182.2	182.2	195	191	191	191
Alloys	T91	HCM12A	HT-9	T91	HCM12A	HT-9	T91	HCM12A	HT-9
Weight gain (mg/dm^2)[b]									
Norm. to 182 h[c]	26.87 ± 2.36	26.04 ± 2.44	27.39 ± 1.85	137.3 ± 4.39	119.94 ± 6.60	129.89 ± 5.54	602.65	481.69	466.14
Oxide thickness (μm)									
Transition	0.60	0.40	0.65	1.40	1.20	1.92	5.65	6.95	6.45
Inner	0.89	0.85	0.83	4.35	4.06	4.74	17.02	15.50	16.00
Outer	1.39	1.14	1.21	6.37	5.31	6.03	24.37	20.53	19.53
Total[d]	2.88	2.39	2.69	12.12	10.57	12.69	48.62	40.98	41.98
Inner/outer thickness	0.64	0.75	0.69	0.68	0.76	0.74	0.69	0.76	0.82
Surface oxide phase	Fe_3O_4	Fe_3O_4	Fe_3O_4	Fe_3O_4	Fe_3O_4	Fe_3O_4	Fe_3O_4	Fe_3O_4	Fe_3O_4
O/M ratio[e]									
Inner layer	0.78	0.76	0.77	1.33	1.38	1.33	1.22	1.35	1.30
Outer layer	1.05	0.97	1.09	1.38	1.26	1.30	1.11	1.32	1.30

Temp. (°C)	500			500		
DO (ppb)	100			300		
Exposure (h)	236	236		182	182	182
Alloys	T91	HCM12A		T91	HCM12A	HT-9
Weight gain (mg/dm^2)[b]						
Norm. to 182 h[c]	123.41	112.15		115.13	105.39	126.41
Oxide thickness (μm)						
Transition	1.50	1.25		1.83	1.55	2.00
Inner	4.45	4.35		3.58	3.32	3.91
Outer	6.65	5.76		5.25	4.68	5.59
Total[d]	12.60	11.36		10.66	9.55	11.50
Inner/outer thickness	0.67	0.76		0.68	0.71	0.70
Surface oxide phase	Fe_3O_4	Fe_3O_4		Fe_3O_4	Fe_3O_4	Fe_3O_4
O/M ratio[e]						
Inner layer	1.51	1.44		1.30	1.27	1.32
Outer layer	1.41	1.39		1.29	1.27	1.37

[a] Deaerated condition.
[b] Weight gain was normalized using Eq. (1).
[c] Values accompanied by errors are an average of two measurements and the error is the spread between them.
[d] Total thickness = outer oxide thickness + inner oxide thickness + transition thickness.
[e] M = Fe + Cr.

change measurements, surface analysis, and cross-sectional analysis. The weight gain of corrosion coupons was measured immediately before and after completion of the test. In most of experiments (at 500 °C with 100 ppb and 300 ppb DO, and at 600 °C deaerated SCW), one sample for each alloy was tested. The experiments at 400 °C and 500 °C deaerated SCW were conducted with two samples of each alloy. In Table 4, the weight gain for these samples is the average of the two measurements and the error is the spread between them. Since the exposure times were different in each experiment, the weight gain was normalized to 182 h using the exponential relations obtained from the time-dependent experiments and fit to the following equation:

$$\Delta W^n = kt, \quad \text{or } \Delta W = (kt)^{1/n}, \tag{1}$$

where w is the weight gain in mg/dm^2, k is oxidation rate constant in mg/dm^2/h, t is the time in h, and $1/n$ is the time exponent. The parameters k and $1/n$ were determined for each alloy at 400 °C and 500 °C.

In order to characterize the oxidation products, corrosion coupons were cut into two pieces for surface and cross-section analyses. Analysis of the oxide morphology was done on an SEM and the oxide crystal structure was analyzed using glancing angle ($\theta = 3°$) X-ray diffraction (XRD). The XRD analysis was performing using Cu $k_{\alpha 1}$ (1.541 Å) X-rays at an angle of 3° to sample surface. The diffracted X-ray signal was collected over an angle theta from 8° to 40°. The d-spacing of the planes measured was calculated correctly using Bragg's law and compared with the standard JCPDS (Joint Committee on Powder Diffraction Standard) files for the identified phases. The second piece was mounted on edge in conductive filler resin and polished down to 0.05 μm with Al_2O_3 powder for scanning electron microscopy (SEM) and energy dispersive spectroscopy (EDS) investigations of cross-section of the oxide film. Electron back-scatter diffraction (EBSD) was employed to characterize the phase distribution and grain morphology in the oxide. The SEM was operated at 20 kV, and the automatic EBSD area scan was performed with a step size of 0.3 μm. To allow identification of the existing phases with the EBSD analytical software, crystallographic data files were established based on the XRD analysis in this work in addition to the available database included in the software.

3. Results

Results for oxide weight gain, thicknesses, composition, morphology, and crystal structure are presented for each alloy under the conditions given in Table 4.

3.1. Weight gain

Corrosion coupon weight gains for each alloy were determined immediately after the tests were completed. The time dependence of weight gain was evaluated at temperatures of 400 °C and 500 °C in deaerated SCW and plotted as a function of time in Fig. 2 (400 °C), and the data is tabulated in Table 5. The data was fit to the power law relation given in Eq. (1). The time exponents obtained from experiments at 400 °C are 0.298 for T91, 0.401 for HCM12A, and 0.291 for HT-9. A power law fit to the 500 °C data in Table 5 yielded time exponents consistent with those at 400 °C, but because there are only 2 data points, the results are not conclusive. These exponents agree with those determined by Was and Allen [13] for HCM12A in 500 °C, deaerated SCW (25 ppb DO), where the time exponent was found to be approximately 0.4. The weight gain given in Table 4 was normalized to 182 h using the power law in Eq. (1). Normalization is required to obtain a common exposure time for the analysis of the temperature

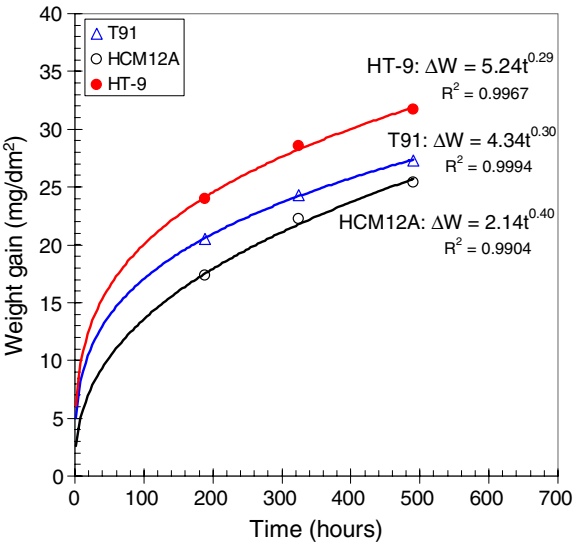

Fig. 2. Time-dependent weight gains of F–M alloys exposed to deaerated SCW at 400 °C. (*Note*: ΔW is weight gain (mg/dm^2) and t is time (h)).

Table 5
Weight gain of F–M alloys at 400 °C and 500 °C as a function of exposure time

Temp. (°C)	Alloy	Weight gain at exposure time (mg/dm^2)			k (mg/dm^2/h)	(1/n)	R^2
		188 h	324.4 h	490 h			
400	T91	20.550	24.306	27.326	4.335	0.298	0.9997
	HCM12A	17.331	22.261	25.399	2.139	0.401	0.9947
	HT-9	24.008	28.525	31.717	5.240	0.291	0.9967
		195 h	343 h	ND			
500	T91	146.074	177.090	ND	24.191	0.341	0.9998
	HCM12A	133.142	168.573	ND	14.706	0.418	0.9996

ND = not determined.

dependence of oxidation. Fig. 3 compares the normalized weight gains at different temperatures for each alloy tested in deaerated SCW. The results indicated that all of the F–M alloys exhibited similar, strong dependencies of weight gain on temperature. The weight gains at 600 °C are 4–5 times those at 500 °C, which are 4–5 times those at 400 °C.

Under conditions where all three alloys were tested, the order of normalized weight gain is different at each temperature. The weight gains at 400 °C were very close in magnitude, but HT-9 exhibited the greatest oxidation rate, followed by T91 and HCM12A. The weight gain was the highest for T91 at 500 °C and 600 °C, while HT-9 and HCM12A exhibited similar weight gain. These results follow the chromium concentration in the alloys. Alloy HT-9 contains the highest chromium content (12% Cr) of the three alloys and T91 has the lowest with HCM12A being intermediate. The effects were clearly observed at temperature 500 °C and 600 °C where the oxidation rates were high. The alloy composition effect was also observed in controlled oxygen environment (Fig. 4) where HCM12A exhibited a lower weight gain than T91 at an oxygen concentration of 10–300 ppb at 500 °C. This effect revealed the fact that Cr, as an alloying element in F–M alloys, formed the protective oxide on the alloy. As a result, increasing the Cr content in the alloy reduces the oxidation rate.

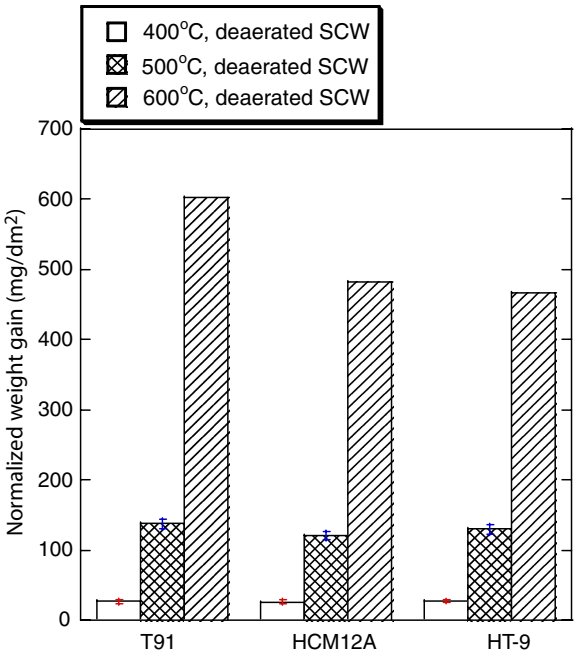

Fig. 3. Normalized weight gain (182 h) of F–M alloys exposed to SCW at 400 °C, 500 °C, and 600 °C deaerated SCW.

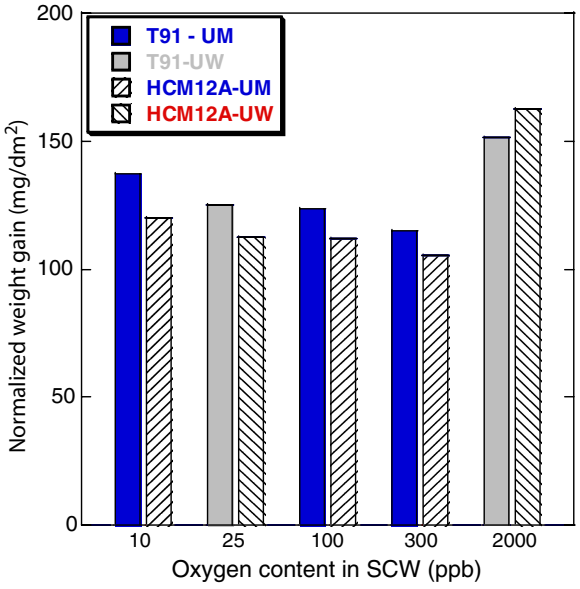

Fig. 4. Comparison of normalized weight gain (182 h) of T91 and HCM12A under SCW condition at 500 °C with oxygen content between 10 and 2000 ppb DO [13]. (*Note*: UM refers to the experiments conducted at the University of Michigan, UW refers to the experiments conducted at the University of Wisconsin).

Fig. 4 shows a comparison of the normalized weight gain as a function of oxygen concentration (10 ppb, 100 ppb and 300 ppb) along with results reported by Was and Allen [13], at 25 ppb and 2000 ppb. The effect of oxygen concentration is small, but the weight gain at 2000 ppb is clearly the highest. The weight gain at 10 ppb DO is next highest, with the values at 25, 100 and 300 ppb falling at decreasing but similar levels. This result is not unexpected, as Dooley et al. [14,15] found that oxygen concentrations of 150–200 ppb resulted in lower weight gains than at either lower or higher oxygen concentrations for F–M alloys used in fossil plants. The authors cited the formation of a two phase, magnetite–hematite structure as the reason for the increased resistance to oxidation at these oxygen concentrations.

3.2. Surface oxide morphology and structure

Planar images of the exposure coupons revealed a rough and porous oxide morphology. Fig. 5 shows the surface oxides on T91, HCM12A and HT-9 following exposure at 400 °C, 500 °C and 600 °C in deaerated SCW, and at 500 °C in SCW containing 300 ppb DO. The oxide formed at 400 °C is granular, with an average grain size of 1–3 μm. At 500 °C, the grain size increased to 2–5 μm and the grain are more porous, as evidenced from the holes in each grain. At 600 °C, the oxide grains were about 5 μm in size and the pore size was smaller than that at 500 °C. These samples contained numerous cracks in the surface oxide. Most of the cracks propagated along the oxide grain boundaries and penetrated deep into oxide layers and stopped at the transition layer. The specimens exposed in 500 °C SCW containing 300 ppb DO showed greater porosity that those exposed to deaerated SCW, Fig. 6.

The structure of the outer oxide layer was determined by glancing angle (3°) X-ray diffraction in order to confine the analysis to the oxide layer. Because of its greater thickness, the specimens from the 600 °C test were investigated using XRD in the θ–2θ mode. The XRD results obtained from all three alloys are similar and those for T91 are shown in Fig. 7. In all cases, at 500 °C and 600 °C, magnetite (Fe_3O_4) is the only phase detected. In fact, the only other phase detected was bcc iron at 400 °C. Because the oxide is considerably thinner at 400 °C than at 500 °C, this is likely due to the metal from the underlying alloy. The high iron content measured in the surface of the outer layer is likely due to metallic iron.

3.3. Cross-sectional analysis

Oxide morphology was investigated on cross-section samples using SEM. The oxide films generally consisted of two layers; an outer layer and an inner layer for all of the alloys. Fig. 8 shows cross-section

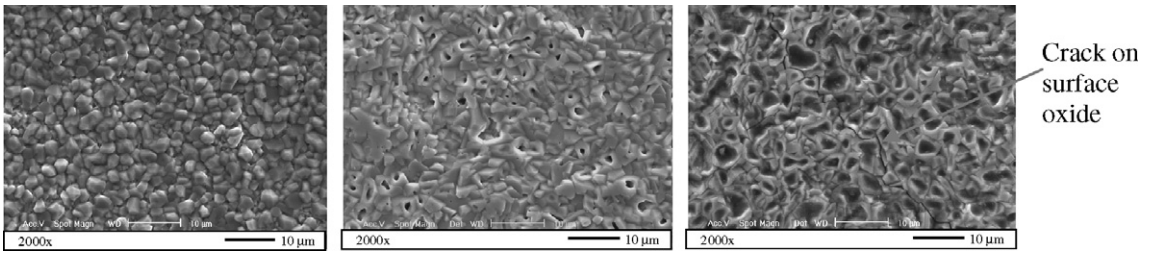

Fig. 5. Oxide morphology of T91 exposed to 400 °C, 500 °C and 600 °C (from left to right) deaerated SCW.

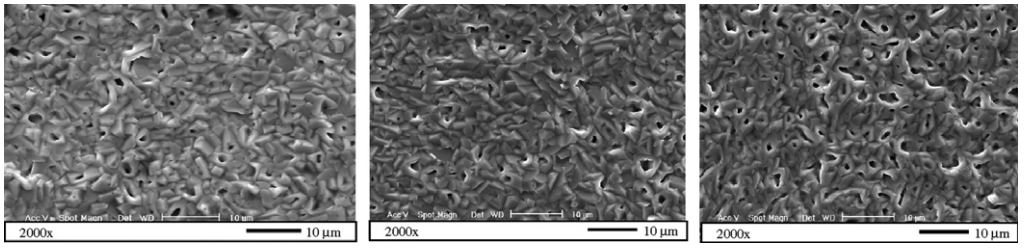

Fig. 6. Planar images of oxide surfaces of T91, HCM12A and HT-9 (from left to right) after exposure to 500 °C SCW containing 300 ppb dissolved oxygen.

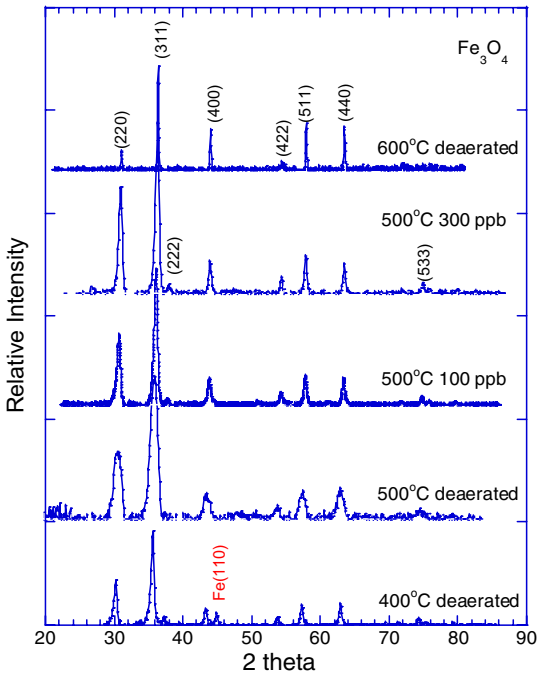

Fig. 7. Glancing angle XRD spectra of the outer oxide layer of T91 tested in SCW at 400 °C, 500 °C deaerated SCW, and at 500 °C + 100 ppb DO and 500 °C + 300 ppb DO. Spectrum of T91 exposed to 600 °C deaerated SCW was measured by θ–2θ Philips Miniflex. All patterns indicated the presence of magnetite (Fe_3O_4) phase.

images of T91 coupons exposed to all environments. The outer layer is characterized by a very rough outer surface and considerable porosity in the columnar oxide grains, in agreement with the planar images. The inner layer is much denser and the interface with the underlying alloy is smooth. At 500 °C, a transition region lies beneath the inner oxide where the metal content increases to bulk values and the oxygen content decreases to nearly zero. This transition zone is difficult to image but appears in backscatter mode in the SEM as having a different morphology from that of the bulk metal or the inner layer. At 600 °C the transition region became more apparent.

The oxide thickness was found to be proportional to the weight gain. The total thickness, determined from transition, inner, and outer layers, shows similar behavior as the weight gain. For example, the total thickness of the 500 °C specimens (10.6–12.7 μm) is ~5 times greater than that of the 400 °C specimens (2.4–2.9 μm), and is less than that of the 600 °C specimens by ~4 times (41–48.6 μm). The ratio of thicknesses of the inner to outer oxide layers is between 0.64 and 0.82 (Table 4). It is interesting to note that the relative thickness is more a function of alloy than of environment. Fig. 9 shows this ratio plotted for each alloy under each of the conditions tested. Note that at 400 °C and 500 °C, alloy HCM12A consistently has the highest ratio (thicker inner oxide) and displays the lowest oxidation rate. Similarly, HT-9 exhibited the highest ratio at 600 °C and corresponds to the lowest weight gain at this temperature.

EDS was used to determine the composition of the oxide layers. The composition profiles show two distinct oxide/metal ratios that correspond to the two oxide layers. The oxygen content is similar in both the outer and inner oxide layers. The outer oxide is predominantly iron oxide whereas the inner layer contains a significant amount of chromium. The transition zone is characterized by a sharp drop in the oxygen content with distance from the inner oxide. The outer oxide has an oxygen-to-metal (O/M) ratio ~1.3, consistent with the composition of magnetite Fe_3O_4, which was identified by XRD. In the inner layer, the O/M ratio is ~1.1–1.3 and is consistent with an iron–chromium oxide, $(Fe,Cr)_3O_4$. Two EDS line scans were performed on each 600 °C sample as shown in Fig. 8(c), where the second scan included the dark region in the transition region. The second scan clearly shows a high concentration of Cr in this region. This chromium-enriched area has an approximate O/M ratio of ~1:1 (Table 6), corresponding to (Fe,Cr)O. In T91, the Mo content in the inner layer is slightly higher than in the outer layer and is closer to the bulk metal value. The same is true for the concentration of Cu and W in HCM12A. Sometimes, a peak in the Cr level can be observed at the interface between the inner and outer layers.

Further analysis was performed using OIM in order to determine the oxide morphology and phase structure that may cause differences in weight gain in controlled oxygen experiments. Fig. 10 illustrates the OIM images of T91 exposed in SCW at 500 °C under deaerated conditions and with 300 ppb DO. The results showed the three major phases; magnetite, Fe–Cr spinel oxide, and α-iron (alloy phase). Magnetite is Fe_3O_4 with an inverse spinel structure. The Fe–Cr spinel oxide corresponds to $(Fe,Cr)_3O_4$. (note that addition of Cr^{3+} tends to transform the inverse spinel to the spinel structure). The outer layer consisted of columnar grains of magnetite (green (1)), the inner layer is a Fe–Cr spinel (yellow (2)) and the alloy substrate is α-iron (red (3)). No hematite (Fe_2O_3) phase was observed in any layer.

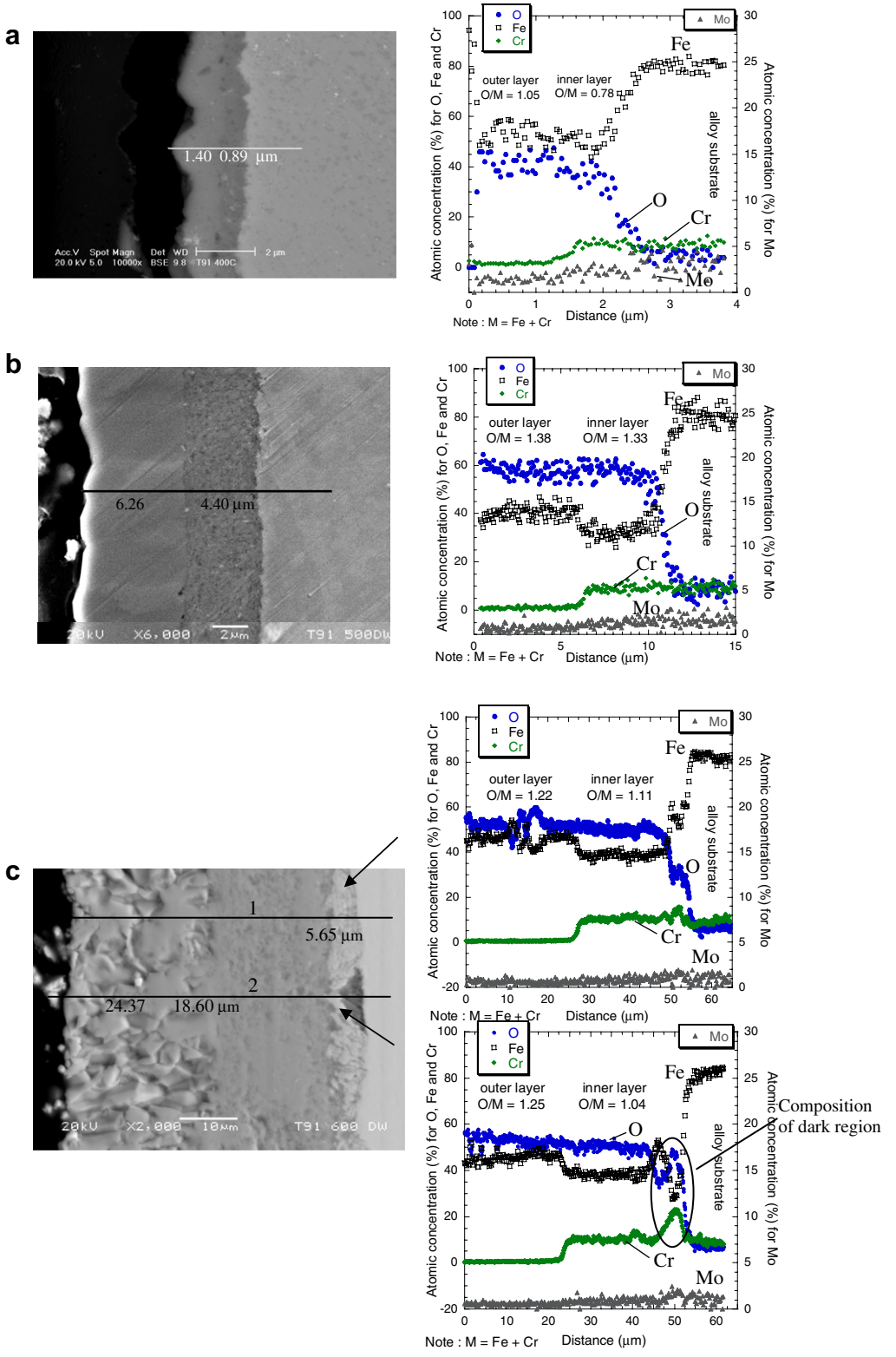

Fig. 8. Oxide composition profiles of T91 exposed to deaerated SCW at (a) 400 °C, (b) 500 °C and (c) 600 °C scanned at line 1 and 2.

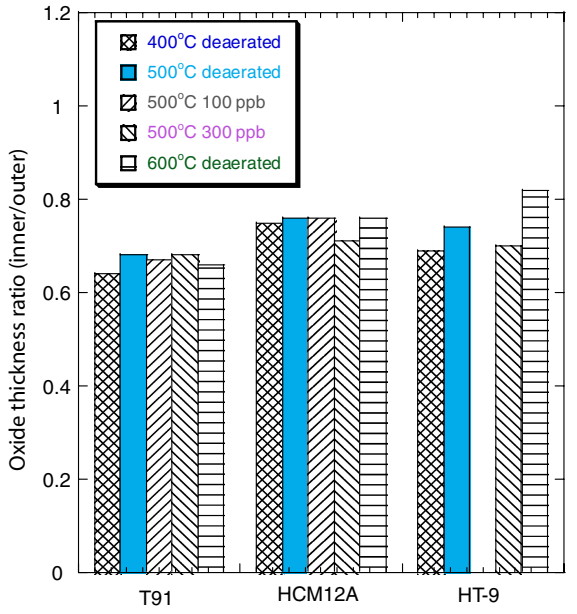

Fig. 9. Comparison of the ratio of the inner and outer oxide layer thicknesses for each alloy after exposure to SCW at the indicated temperature and DO concentration.

Table 6
EDS analysis results of Cr-enriched regions in the transition layer in T91, HCM12A and HT-9 following exposure in deaerated 600 °C SCW for 191 h

Alloy	O	Fe	Cr	O/M
T91	44.16	31.50	22.37	0.82
HCM12A	48.93	23.52	23.33	1.07
HT-9	49.07	30.30	19.13	0.99

Significant differences in the average grain size in the magnetite layer were found between the two oxygen levels. The average oxide grain size was 0.75 μm in the deaerated condition, 1.89 μm in the 100 ppb DO condition and 1.84 μm in the 300 ppb DO condition. Due to the low quality of the EBSD patterns from the Fe–Cr spinel layer, the grain size could not be determined.[1]

4. Discussion

4.1. Effect of composition

Chromium content is known to significantly affect the oxidation behavior of F–M alloys in non-SCW conditions. Cho [10] showed that generally, the higher the Cr content, the lower the oxidation rate. Additionally, the presence of a small amount of chromium results in the formation of a chromium-rich iron oxide, and at higher chromium concentrations, an iron–chromium spinel forms. The Fe–Cr spinel is much denser and it is believed to provide better oxidation resistance than the porous magnetite outer layer [10]. Aside from Cr, other alloying elements that have been reported to affect the oxidation rate are Si, Ti, V and W [16,17]. Fry et al. [18] showed that silicon improves the steam oxidation resistance but enhances the agglomeration of carbides. The addition of Ti and Y further improves the oxidation resistance of the alloy [19]. A comparison of the oxidation of T91 (with V) and T92 (with V and W) and 9Cr1Mo alloys in steam shows that either V or W are detrimental to steam oxidation resistance [20]. Among the F–M alloys in this study, HT-9 contains the highest chromium (11.63%), followed by HCM12A (10.83%), and T91 (8.37%). The Si concentration in these three alloys are similar; 0.28, 0.27 and 0.22 for T91, HCM12A and HT-9, respectively. Only HT-9 contains trace of Ti (<0.01%). T91 and HCM12A contain ~0.2% V, and HT-9 contains ~0.3% V. The W content in HCM12A is 1.89% and in HT-9 is 0.52%. Thus, the only minor alloying element that varies in content between the three alloys and could affect the oxidation behavior is W, and overall, the major differences between these three F–M alloys is in the chromium concentrations.

The results of the weight gain measurements showed that T91 has the highest weight gain at 500 °C and 600 °C, and HT-9 and HCM12A exhibited similar weight gains. This behavior follows the chromium content of the alloys. The weight gains at 400 °C were very similar, but HT-9 exhibited the greatest oxidation rate, followed by T91 and HCM12A. It is possible that at the lower temperatures, other factors affect the oxidation rate. Mongomery et al. [20] showed that the oxidation rate of coarse grain alloys tend to be faster than that of a fine grain alloy for 17% Cr alloys undergoing steam oxidation. Since HT-9 has the largest grain size (~50 μm), followed by HCM12A (~13.5 μm) and T91 (~10 μm), the 400 °C result could be explained by the microstructure. However, composition is more important at higher temperature. For example, at 600 °C, the oxidation rate of HT-9 is less than that of HCM12A, which could be due to the higher W content in HCM12A and the higher Cr content in HT-9.

[1] For interpretation of color in Fig. 10, the reader is referred to the web version of this article.

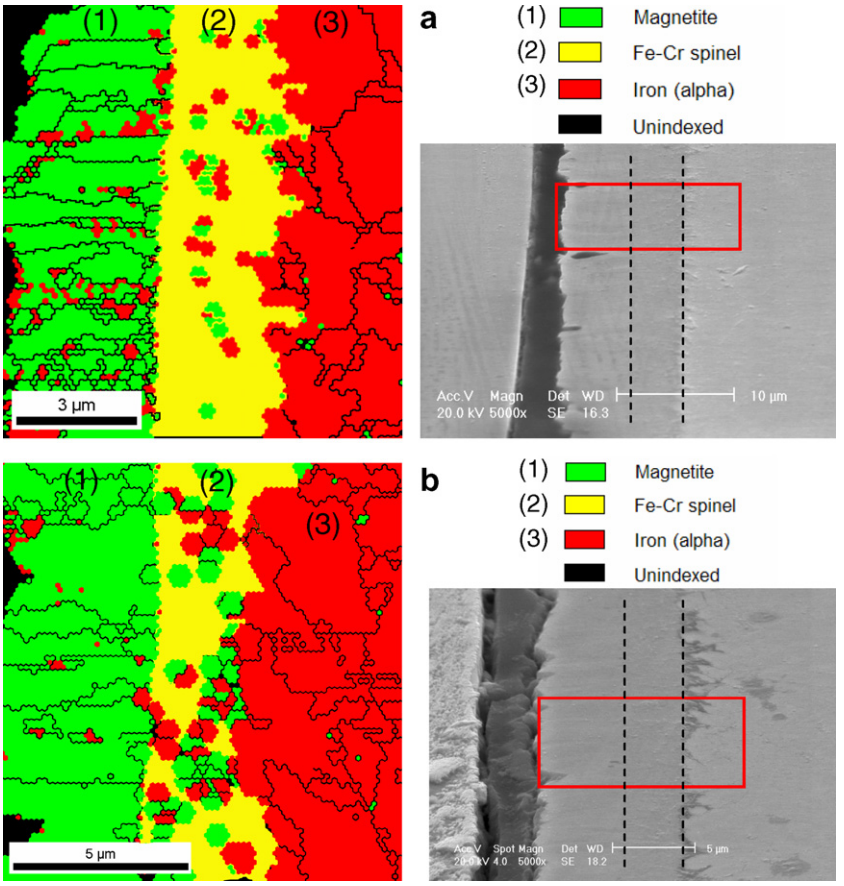

Fig. 10. OIM images of T91 exposed to SCW at 500 °C under (a) deaerated condition and (b) 300 ppb. The outer layer consists of columnar grain of magnetite (1), the inner layer is a Fe–Cr spinel (2), and the alloy substrate is α-iron (3).

4.2. Temperature dependence of oxidation

Temperature has a great influence on the oxidation rate of F–M alloys in SCW as shown in Fig. 3. The temperature dependence can be fit by an Arrhenius equation;

$$k = k_0 \exp(-Q/RT), \tag{2}$$

where k and k_0 are rate constants (mg/dm^2/h), Q is the activation energy of the oxidation reaction (J/mol), R is the gas constant (8.314 J/mol-K) and T is the temperature (K). Substituting Eq. (2) into Eq. (1) gives the weight gain as a function of time and temperature

$$\Delta W = k_{\text{eff}} \exp(-Q/nRT) t^{1/n}, \tag{3}$$

where k_{eff} is the effective oxidation rate constant (mg/dm^2/h).

For a constant exposure time the activation energy for oxidation, Q, can be obtained from the

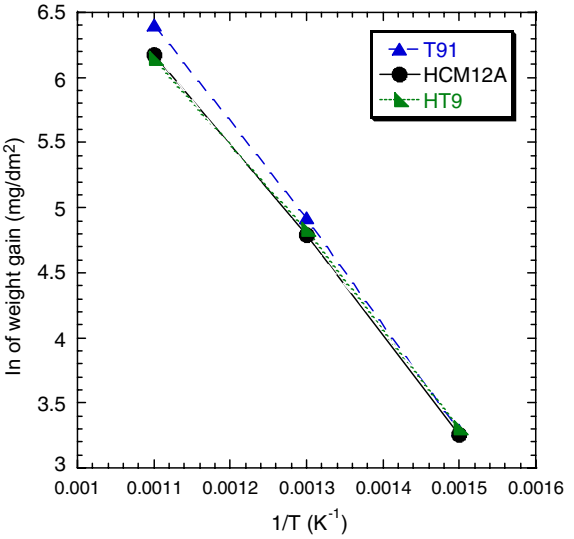

Fig. 11. Plots of ln ΔW vs. $1/T$ for T91, HCM12A and HT-9 in deaerated SCW.

Table 7
Activation energy of for F–M alloys oxidation under similar conditions

Alloys	Experimental conditions	Activation energy (Q) (kJ/mol)	Ref.
21/4Cr-1Mo	Air at 600–800 °C	290	[21]
T91	Steam at 300–600 °C	199	[16]
T91	Steam at 400–650 °C	207.9	[22]
T91	SCW at 400–600 °C	**189.29**	**This study**
HCM12A	Steam at 300–600 °C	166	[16]
HCM12A	SCW at 400–600 °C	**177.14**	**This study**
HT-9	SCW at 400–600 °C	**172.60**	**This study**

slope of a plot of ln ΔW vs. $1/T$. Fig. 11 presents plots of ln ΔW vs. $1/T$ for the three F–M alloys following tests in deaerated 400 °C, 500 °C and 600 °C SCW. Table 7 gives the calculated activation energies of the F–M alloys from this study compared to values obtained from the literature under different conditions [16,21,22]. Note that the activation energies of HCM12A and HT-9 in SCW are very close and below that of T91. Moreover, the values for a given alloy are in quite similar in both steam and SCW.

Oxidation can occur by one of two processes; anion (Fe^{+}) diffusion through the oxide to the oxide–water interface, or cation (O^{-}) diffusion through the oxide to the metal-oxide interface. The activation energy provides a clue as to which process is rate controlling. Table 8 presents selected diffusion data of ions in oxide from literature [23–32].

The activation energies presented in Table 8 are classified into three groups, diffusion of anions (oxygen) and cations (iron and chromium) in metal oxides, and diffusion along the grain boundary. The data on oxygen diffusion in magnetite is quite scattered. The diffusion data from hydrothermal experiments showed particularly low values of Q of ~188 and 71 kJ/mol [26,27]. Because the nature of the hydrothermal condition may change the defects in magnetite, the Q values from these experiments may be affected (hydrothermal experiments were conducted under water pressures of 10, 100, or 200 MPa). Data on the diffusion of oxygen in the spinel structure oxides $Fe_{2.32}Ni_{0.68}O_4$ and $NiCr_2O_4$, showed higher values of Q (255 and 295 kJ/mol) than in the case of magnetite, implying that the diffusion in the Fe-metal oxide spinel is slower and results in a reduction of the oxidation rate. The data for grain boundary diffusion of oxygen is the lowest, 167 kJ/mol [24]. It was also reported in reference [24–27] that experimental values of oxygen diffusivity were relatively lower than the theoretical values by 1.5–2 times. The reason for the difference was attributed to the higher diffusion rate through porous morphology of magnetite layer.

Table 8
Selected diffusion data in metal oxides in comparison with experimentally determined activation energies

Diffusing ions	Temperature (°C)	Frequency factors (D_o) (cm^2/s)	Activation energy (Q) (kJ/mol)	Ref./note
Oxygen				
Oxygen in Fe_2O_3	1150–1250	10^{-11}	610	[23]
Oxygen in Fe_3O_4	480–1100	1.2×10^{-9}	264	[24]
Oxygen in Fe_3O_4	505–660	4.3×10^{-7}	211	[25]
Oxygen in Fe_3O_4	500–800	3.5×10^{-6}	188.4	[26] 20–200 MPa hydrothermal
Oxygen in Fe_3O_4	302–550	3.2×10^{-14}	71	[27] hydrothermal
Oxygen in Fe_3O_4	450	10^{-21}		[29]
Oxygen in $Fe_{2.32}Ni_{0.68}O_4$	1140–1340	5×10^{-7}	255	[28]
Oxygen in $NiCr_2O_4$	1200–1500	2.6×10^{-8}	295	[29]
GB diffusion in Fe_3O_4	480–1100	1.2×10^{-2}	167	[24][a]
Iron				
Iron in Fe_3O_4	0–80	–	87.9	[30] nanoparticles
Iron in Fe_3O_4	450	10^{-15}	149.1	[31]
Iron in Fe_3O_4	350–1200	2×10^{-14} (cal.) 5×10^{-12} (meas.)	238	[32]
Iron in Fe_3O_4	750–1000	5.2	230	[23]
Iron in $Fe_{0.92}O$	690–1010	0.014	126.4	[23]
Cr in Cr_2O_3	1000–1350	4000	420	[23]

[a] Diffusivity of oxygen in GB of Fe_3O_4 was calculated from $\delta D = 1.2\times10^{-15}\exp(-167\text{ kJ/mol/RT})\ m^3s^{-1}$ [24] and assuming grain boundary thickness $\delta = 10^{-9}$ m.

Experimental values for the diffusion coefficient of iron in magnetite also vary considerably. However, overall cation diffusion is greater than oxygen diffusion in magnetite [23,24]. Atkinson [32] noted that the observed oxidation rate of iron in steam is consistent with the iron diffusion rate in magnetite. The data on chromium diffusion is limited. However, it tends to be slower than iron.

In summary, the activation energy for diffusion of oxygen and iron in magnetite are similar and greater than 200 kJ/mol. From the data in Table 8, the average activation energy for diffusion in magnetite is around 211–264 kJ/mol for oxygen diffusion, and 230–238 kJ/mol for iron diffusion. In the Cr-rich spinel, the activation energy tends to be higher. The measured activation energy for oxidation for the F–M alloys in this study is ~172–189 kJ/mol, which is less than the activation energies for oxygen and iron diffusion, but similar to that for grain boundary diffusion of oxygen (167 kJ/mol). This suggests that the likely controlling mechanism is a short circuit diffusion process for oxygen through the inner, more protective layer.

Calculation of the diffusion distances for iron and oxygen was performed to characterize the relation of diffusion distances and oxide layer thickness, and to support the above assumptions. The diffusion distances were calculated as follows;

$$x = \sqrt{4Dt}, \tag{4}$$

where x is diffusion distance (cm), D is diffusion coefficient (cm^2/s), and t is time (s).

Using the limited data on diffusivities of these ions, the diffusion distances were calculated in three groups; (1) oxygen diffusion in magnetite, (2) iron diffusion in magnetite, and (3) oxygen diffusion along grain boundaries of magnetite or other spinel. Fig. 12 displays the calculated distances compared with the inner oxide layer thickness at temperatures between 400 °C and 600 °C. Because of the greater density and slower diffusion in the Cr-rich spinel, diffusion through the inner layer is likely the rate limiting process. The plots show that all of diffusion distances of ions are smaller than the oxide thickness, but the diffusion distance via grain boundaries is closest.

4.3. Time dependence of oxidation rate

The weight gain of F–M alloys exposed to SCW environment increases as a function of time following the power law, Eq. (1). This behavior results from the diffusion of ions through a compact layer of the oxide. As the oxide grows thicker, the diffusion distance increases, and the oxidation rate slows. Theoretically, oxidation should follow parabolic ($1/n = 0.5$) behavior [23] if (i) the oxide scale is compact and adherent, (ii) diffusion of ions through the scale is the rate-controlling process, (iii) thermodynamic equilibrium exists at both the metal/oxide and oxide/gas interfaces, (iv) the oxide deviates only slightly from stoichiometry, and (v) oxygen solubility in the metal may be neglected.

Fits of the data at 400 °C yield a time exponent that deviates from a parabolic rate law. The time

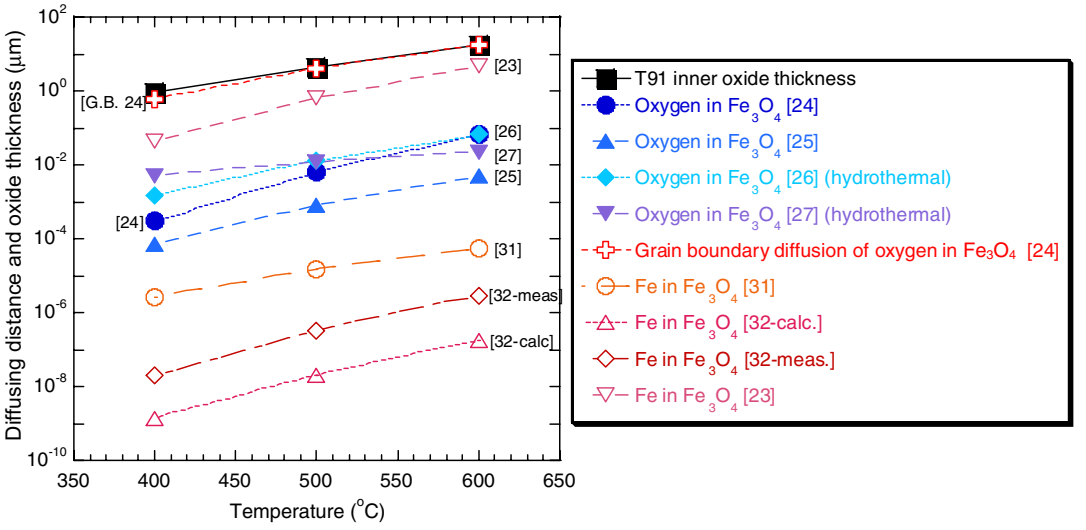

Fig. 12. Diffusing distances of oxygen and iron ions in magnetite compared to thicknesses of inner layer (Fe–Cr spinel) of T91.

exponents are in the range 0.29–0.40 at 400 °C and 0.34–0.42 at 500 °C. Even though the range of exposure times in this study is rather short (200–500 h), these exponents agree with relation developed by Was and Allen [13] for HCM12A in 500 °C, deaerated SCW (25 ppb DO), and with data for 12Cr–1MoVNb and 9–11Cr–WVTa alloys exposed in the loop in Studsvik R2 reactor in Sweden. The exposure time in Allen's work ranged from 200 to 1000 h and the reported time exponent is 0.4. Note that the average time exponent at 400 °C in this study is slightly less than that of the experiment at 500 °C. These values imply slower oxidation kinetics at 400 °C.

Deviation from the expected parabolic kinetics of parabolic law is probably caused by the microstructure of the oxide film, which is neither homogeneous nor uniform [33–35]. The parabolic law is derived from the transport of either vacancies or interstitials of ions through a uniform oxide film. In practice, the films are highly defective and contain pores, cracks and grain boundaries. In the case of crystalline oxides, the grain boundary may behave as a diffusion short circuit path. As a result, the effective diffusivity may be determined by the defect state of the oxide and the time dependence may deviate from a parabolic law.

4.4. Dissolved oxygen effect

The effect of dissolved oxygen was determined by varying the oxygen concentration in the system. The weight gain for all the alloys studied was clearly the highest at 2000 ppb. The weight gain at 10 ppb DO is next highest, with those at 25, 100 and 300 ppb falling at intermediate values, with a minimum at 300 ppb. The trend of weight gain agreed with Dooley et al. [14,15] who found that an oxygenate treatment (OT) with oxygen concentrations of 30–150 ppb in fossil plants resulted in lower weight gains than at either lower or higher oxygen levels. The author suggested that the formation of FeOOH or Fe_2O_3 on the iron-based alloy surface is beneficial in reducing the oxidation rate. These two oxides not only covered the surface, but also permeated down the pores of the magnetite and hence reduce the rate of oxygen diffusion in the scale. Hematite formation on T91 was also reported by Was and Allen [13] in an experiment in 2000 ppb DO, and by Laverde et al. [22] for cyclic oxidation of T91 tested in steam. Laverde also noted that hematite formation was observed clearly after exposure time ~2–3 weeks.

The results of line-scan composition profiles from tests in 500 °C with 100 and 300 ppb DO did not reveal any other phases besides magnetite and a Fe–Cr spinel. The oxide phases and grain size were further analyzed by OIM, and the results showed that three major phases, magnetite, a Fe–Cr spinel oxide and α-iron (alloy phase) were present. No hematite was observed in any layer. However, significant variations in the average grain size of the magnetite with dissolved oxygen concentration were found. The average magnetite grain size on the samples exposed under deaerated conditions was about half that at 100 and 300 ppb DO. This result may provide some insight into the difference in oxidation rates. The activation energy suggested that the short circuit diffusion of oxygen in magnetite, such as along grain boundaries, may control the oxidation rate. The smaller grain size in the deaerated condition may provide for easier oxygen diffusion to the inner layer, and result in a higher growth rate.

4.5. Oxide morphology and structure

The morphology and structure of the oxide layers can have the important effects on oxidation if oxygen diffusion along grain boundaries and defects controls the oxidation rate. The outer layer is formed by outward diffusion of iron ions and reaction with water at the oxide–water surface, creating columnar grains of magnetite. The magnetite layer contains high porosity, thus enhancing the effective diffusivity. Magnetite was formed since it is the most stable oxide at this temperature range (400–600 °C) presumable based on thermodynamic. The inner layer has a denser structure and also acts as a protective oxide film. The inner oxide is $(Fe,Cr)_3O_4$ spinel oxide and likely forms by inward diffusion of oxygen to the oxide–metal interface. At 600 °C, (Fe, Cr)O regions form at the oxide–metal interface, that corresponding to wustite (MO) formation; wustite is stable above 570 °C.

At thermodynamic equilibrium, the type of oxide formed depends on the partial pressure of oxygen. The sequence of oxides can be predicted, with the most oxygen-deficient oxide contacting the metal and the most oxygen-rich oxide next to the SCW interface. In the Fe-O system, the oxide sequence from innermost to outermost is $FeO–Fe_3O_4–Fe_2O_3$ [23]. However, not all of oxides are stable at a given temperature and so they may not be present in the

scale. Wustite (FeO) is predicted to be stable at temperature above 570 °C. The calculated oxygen partial pressure versus metal oxide composition of Fe–Cr–O at 500 °C by FactSage© [36] is given in Fig. 13. This diagram shows that for the three F–M alloys, magnetite (Fe_3O_4) and an Fe, Cr spinel (M_3O_4, with M = Fe + Cr) will form at P_{O_2} levels of $\sim 10^{-19}$–10^{-14} atm. The presence of these oxide phases was confirmed by the EDS analysis of the oxide layers. At higher oxygen partial pressure, the stable oxide phases have the corundum (M_2O_3) and spinel (M_3O_4) structures.

The relative thicknesses of the inner and outer oxide layers should be proportional to the relative diffusion rates that generate each layer [37]. The ratio of the inner to outer oxide layer thicknesses is slightly less than one, implying that the diffusion rates for ions that create the inner layer (O ions) should be slightly less than those that create the outer layer (Fe ions). Moreover, it is interesting to note that the ratio of the thickness of the inner to outer oxide layers is more a function of alloy than of environment. The ratio is inversely proportional to the weight gain under each of the test conditions, suggesting that the inner layer serves as the protective oxide. The diffusion rate of ions through this layer is slower than diffusion through the magnetite

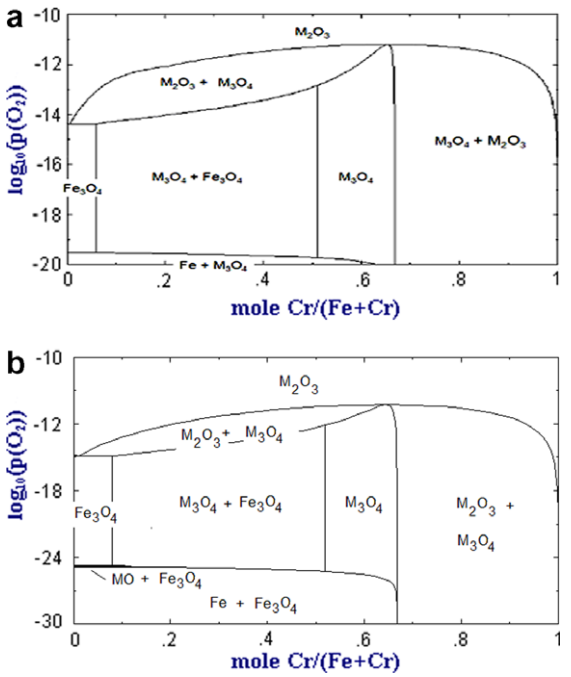

Fig. 13. Calculated oxygen partial pressure (atm) versus composition diagram of the Fe–Cr–O ternary system at (a) 500 °C and (b) 600 °C using the FactSage© [36] program. M is Fe + Cr.

layer. As a result, the oxidation rate is less for alloys that have a higher inner to outer oxide ratio.

Oxide cracking was observed after exposure to 600 °C deaerated SCW. The cracking likely resulted from the thermal expansion mismatch of oxide and alloy on cooling. The calculated volume change of magnetite after cooling from 600 °C is ~1.28%, which is twice that for the alloy, ~0.69%. (α for magnetite = 20.6×10^{-6}/K (293–843 K) and 50.1×10^{-6}/K (843–1273 K) [38], and F–M alloy = 11.9×10^{-6}/K [39].) Since the samples from this test exhibited very thick oxides, the tensile stress generated in oxide will be high enough to cause the microcracks.

4.6. Oxidation mechanism

The oxidation mechanism of F–M alloys in SCW is likely due to two processes that are specific to the two layers of the oxide. The porous outer layer forms by the diffusion of iron ions through the Fe–Cr spinel and magnetite layers to the oxide–water interface where an oxidation reaction occurs that accounts for the growth of the outer layer. Iron has a higher diffusion coefficient than Cr in both the oxide and metal phases [33]. However, iron diffusion is likely aided by the heavily defected structure of the magnetite and is therefore, not rate limiting.

The inner Cr-rich spinel oxide grows by the inward diffusion of oxygen to the oxide–metal interface. The highly defected outer layer allows for rapid oxygen inward diffusion through the magnetite. The inner layer is denser and the volume diffusion of oxygen is far too slow to account for the rate of oxide growth. Rather, short circuit diffusion of oxygen, possibly by grain boundaries in the oxide, or other defects, increases the effective diffusion coefficient. The relatively good agreement between the activation energies for oxidation in the F–M alloys and that for grain boundary diffusion of oxygen supports a short circuit process for oxygen diffusion to the oxide–metal interface.

5. Conclusion

Among the candidate alloys for use in a SCWR, F–M alloys exhibited relatively high weight gain compared to austenitic or nickel-base alloys. Of the F–M alloys studied, T91 experienced the highest weight gain, followed by HCM12A and then HT-9. This trend shows that the increment of Cr content has a significant effect on oxidation rate.

The oxides were characterized by a two layer structure in which the outer layer consisted of columnar magnetite that was very porous with a rough exterior surface. The inner layer is a Fe–Cr spinel oxide and was much denser than the outer layer. The inner layer thickness was slightly less than the outer layer thickness and the ratio of the inner layer and outer layer thickness was greatest for the alloy that showed the lowest weight gain. Beneath the inner layer was a transition zone in which the oxygen concentration rapidly drops to near zero, and the thickness of the transition zone increases with temperature and DO concentration in the SCW.

The weight gain vs. time for F–M alloys exposed to SCW follows a power law behavior with a time exponent between 0.3 and 0.4. Temperature has a strong influence on the oxidation behavior of F–M alloys in SCW. Oxide weight gain follows an Arrhenius behavior. The activation energies were in the range ~172–189 kJ/mol for all alloys, implying a short circuit diffusion mechanism for oxygen through the inner layer. At 600 °C, cracking of the oxide can lead to direct contact between water or oxygen and the alloy substrate. The dissolved oxygen concentration in the water was a secondary factor with the highest weight gain observed at 2000 ppb DO, followed by <10, 25, 100 and 300 ppb DO. The morphology of the magnetite film suggests that the cause for the reduction in weight gain is the smaller grain size of the magnetite, allowing short circuit diffusion of oxygen.

In SCW, diffusion of oxygen appears to control the oxidation mechanism. The inner oxide layer (Fe–Cr spinel oxide) was formed by a solid-state reaction between oxygen diffusing through the layer and reacting at the oxide–metal interface. The outer (magnetite) layer was formed by diffusion of iron ions outward and reaction with water at the oxide surface. However, the oxidation rate-controlling process is likely the diffusion of oxygen through the inner Fe–Cr oxide layer.

Acknowledgement

Support for this work was provided by the United States Department of Energy under the I-NERI Project (contract number 3F-01041).

References

[1] A Technology Roadmap for Generation IV Nuclear Energy Systems, Report No. GIF002-00, December 1, 2002. <http://nuclear.gov>.
[2] Y. Oka, S. Koshizuka, in: Proceeding of SCR-2000, Nuclear Engineering Research Laboratory, University of Tokyo, 2000, Paper 203, ISBN 4-901332-00-4.
[3] Y. Ikushima, in: Proceeding of SCR-2000, Nuclear Engineering Research Laboratory, University of Tokyo, 2000, Paper 202, ISBN 4-901332-00-4.
[4] L.B. Kriksunov, D.D. Macdonald, J. Electrochem. Soc. 142 (12) (1995) 4069.
[5] R.M. Latanision, Corrosion 51 (4) (1995) 270.
[6] P. Kritzer, N. Boukis, E. Dinjus, Corrosion 51 (41) (1995) 29.
[7] S. Kasahara, J. Kuniya, K. Moriya, F. Kano, S. Shiga, H. Takahashi, in: Proceeding of ICAPP, American Nuclear Society, 2003, Paper 3293.
[8] S. Kasahara, J. Kuniya, K. Moriya, N. Saito, S. Shiga, in: GENES4/ANP2003, Atomic Energy Society of Japan, 2003, Paper 1132.
[9] H.S. Cho, A. Kimma, S. Ukai, F. Fujiwara, J. Nucl. Mater. 329–333 (2004) 387.
[10] G.S. Was, S. Teysseyre, J. McKinley, in: Proceeding of Corrosion 2004, NACE International, 2004, Paper 04492.
[11] G. Gupta, B. Alexandreanu, G.S. Was, Metall. Mater. Trans. 35A (2) (2004) 717.
[12] K.E. Wardle, J.I. Cole, US Department Energy J. Undergraduate Res. 3 (2003).
[13] G.S. Was, T.R. Allen, Time, temperature, and dissolved oxygen dependence of oxidation of austenitic and ferritic–martensitic alloys in supercritical water, in: Proceeding of ICAPP 2005, American Nuclear Society, 2005.
[14] B. Dooley, B. Larkin, L. Webb, F. Pocock, A. Bursik, Oxygenated treatment for fossil plantsProceedings of 16th International Water Conference, vol. 53, Engineers Society of Western Pennsylvania, 1992.
[15] B. Dooley, J. Mathews, R. Pate, J. Taylor, Ultrapure-water (July/August) (1995) 48.
[16] R.L. Klueh, D.R. Harries, High Chromium Ferritic and Martensitic Steels for Nuclear Applications, ASTM, PA, 2001, p. 122–134.
[17] N.J. Simms, J.A. Little, Mater. Sci. Technol. (1989) 1133.
[18] A. Fry, S. Osgerby, M. Wright, Oxidation of Alloys in Steam Environments – Review, NPL Report MATC(A)90, The UK's National Measurement Laboratory, 1990.
[19] F. Abe, M. Igarashi, S. Wanikawa, M. Tabuchi, T. Itagaki, K. Kamura, K. Yamaguchi, R&D of advanced ferritic steel of 650 °C USC boilers, in: A. Strang, W.M. Banks, R.D. Conroy, G.M. McColvin, J.C. Neal, S. Simpson (Eds.), Proceedings of the 5th International Charles Parsons Turbine Conference, IOM Communications Ltd., 2000, p. 129.
[20] M. Mongomery, A. Karlsson, Survey of Oxidation in Steamside Conditions, VGB Kraftwerkstechnik, 1995, p. 230.
[21] L. Marino, L.O. Bueno, J. Pressure Vessel Technol. 123 (2001) 88.
[22] D. Laverde, T. Gómez-Acebo, F. Castro, Corros. Sci. 46 (2004) 613.
[23] ASM HandbookCorrosion: Fundamentals, Testing, and Protection, vol. 13A, ASM International Materials Park, OH, 2003, p. 97.
[24] A.G. Crouch, J. Robertson, Acta Metall. Mater. 38 (12) (1990) 2567.
[25] Z.D. Sharp, Geology 19 (6) (1991) 653.
[26] B.J. Giletti, K.C. Hess, Earth Planet. Sci. Lett. 89 (1988) 115.

[27] J.E. Castle, P.L. Surman, J. Phys. Chem. 71 (13) (1967).
[28] H.M. O'Bryan, F.V. DiMarcello, J. Am. Ceram. Soc. 53 (1970) 413.
[29] W.D. Kingery, D.C. Hill, R.P. Nelson, J. Am. Ceram. Soc. 43 (1960) 473.
[30] M. Myers, J. Phys. Chem. 107 (30) (2003) 7501.
[31] L. Himmel, R.T. Mehl, C.E. Birchenall, J. Metals 5 (1953) 827.
[32] A. Atkinson, M.L. O'Dwyer, R.I. Taylor, J. Mater. Sci. 18 (1983) 2371.
[33] A.S. Khanna, High Temperature Oxidation and Corrosion, ASM International, 2002, p. 20–37.
[34] D. Gupta, A.D. Romig, M.A. Dayananda, Diffusion processes in high technology materials, in: Proceedings of the ASM symposium, Trans tech publications Ltd., Switzerland, 1988, p. 1.
[35] B. Bokstein, N. Balandina, Grain boundary diffusion and grain boundary segregation, in: Proceedings of the International Workshop DiBoS-97, Scitec Publications Ltd., 1998.
[36] FactSage, ©1976–2004, ThermFact Inc. & GTT-Technologies.
[37] Metals Handbook, Corrosion, ninth edition., ASM International Handbook committee, Metals Park, OH, 1987.
[38] A Handbook of Physical Constants, Mineral Physics and Crystallography, AGU reference, the American Geophysical Union, 1995, p. 29.
[39] J. Robertson, M.I. Manning, Mater. Sci. Technol. 6 (1990) 81.